Absence of Ce^{3+} Sites in Chemically Active Colloidal Ceria Nanoparticles

Jean-Daniel Cafun,[†] Kristina O. Kvashnina,[†] Eudald Casals,[‡,§] Victor F. Puntes,[‡,§,*] and Pieter Glatzel[†,*]

[†]European Synchrotron Radiation Facility (ESRF), BP 220, 6 Rue Jules Horowitz, 38043 Grenoble, France, [‡]Institut Català de Nanotecnologia (ICN), Campus UAB, 08193 Bellatera, Spain, and [§]Universitat Autònoma de Barcelona (UAB), Campus UAB, 08193 Bellaterra, Spain

ABSTRACT The catalytic performance of ceria nanoparticles is generally attributed to active sites on the particle surface. The creation of oxygen vacancies and thus nonstoichiometric $CeO_{2-\delta}$ has been proposed to result in Ce^{3+} sites with unpaired f electrons which can be oxidized to spinless Ce^{4+} ions during catalytic reactions. We monitored the Ce electronic structure during the synthesis and catalase mimetic reaction of colloidal ceria nanoparticles under *in situ* conditions. By means of high-energy resolution hard X-ray spectroscopy, we directly probed the Ce 4f and 5d orbitals. We observe pronounced changes of the Ce 5d bands upon reduction of the particle size and during the catalytic reaction. The Ce 4f orbitals, however, remain unchanged, and we do not observe any significant number of spin-unpaired Ce^{3+} sites even for catalytically active small (3 nm) particles with large surface to bulk ratio. This confirms strong orbital mixing between Ce and O, and the Ce spin state is conserved during the reaction. The particles show an increase of the interatomic distances between Ce and O during the catalytic decomposition of hydrogen peroxide. The redox partner is therefore not a local Ce^{3+} site, but the electron density that is received and released during the catalytic reaction is delocalized over the atoms of the nanoparticle. This invokes the picture of an electron sponge.

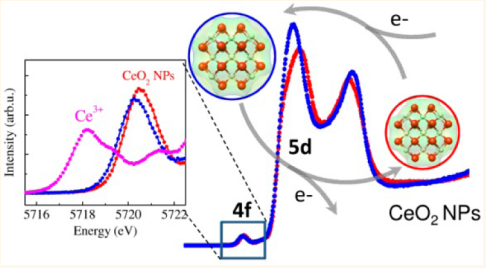

KEYWORDS: ceria nanoparticles · electronic structure · catalytic activity · *in situ* spectroscopy · spin-pairing

The widely used capacity to store and release oxygen in their intrinsic n-type fluorite structure provides materials based on ceria (CeO_2) with unique redox properties that open new possibilities for promising applications in the areas of catalysis,[1−3] fuel cells,[4,5] and biomedicine.[6,7] The redox properties of ceria are closely linked to the crystal structure which, in turn, depends on the synthesis process.[8] Developing good CeO_2 materials for industrial applications involves a clear understanding of the chemical activity of CeO_2 which ultimately depends on electronic structure, which at the nanoscale is controlled by the morphology. Reducing the size of CeO_2 to the nanometer scale enhances the chemical activity.[3,9] The generally advocated mechanism states that particle miniaturization results in an increase of the surface to bulk ratio and thus significantly nonstoichiometric $CeO_{2-\delta}$ owing to surface oxygen vacancies. Electrons left behind by O vacancy formation reduce Ce^{4+} to Ce^{3+} ions,[10,11] resulting in a higher level of catalytically active Ce^{3+} ions at the surface that are responsible for the increased chemical activity of nanoceria when compared to bulk ceria.[12] This ionic description of the catalytic activity is commonly supported by experiments performed under conditions that are very different from the environment of the working catalyst and may even change the chemical state of ceria (*e.g.*, high vacuum).[13] The electronic structure of ceria NPs critically depends on the reaction environment, thus experiments need to be performed under *in situ*/*operando* conditions to fully reproduce the environment under which NP activity is observed.

We monitored the electronic structure of ceria NPs using high-energy resolution fluorescence-detected hard X-ray absorption spectroscopy (HERFD-XAS). Such inner-shell spectroscopy provides an element-selective probe of the electronic state that is compatible with *in situ* conditions. High-energy resolution XAS furthermore allows observing spectral features beyond the limitation of the L_3 edge lifetime broadening.[14,15] Enhanced spectral resolution provides the basis for the observations that are reported here (Figure 1).

* Address correspondence to pieter.glatzel@esrf.fr, victor.puntes@icn.cat.

Received for review July 11, 2013 and accepted November 5, 2013.

Published online November 12, 2013
10.1021/nn403542p

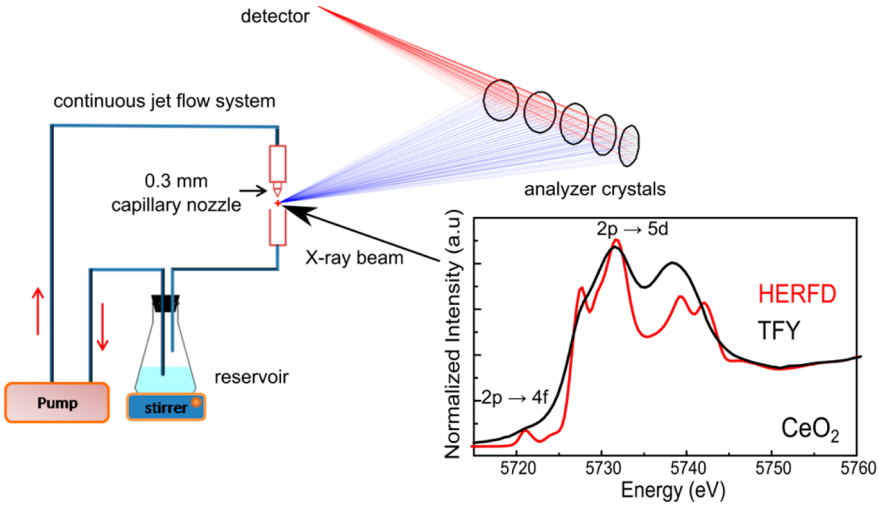

Figure 1. Experimental setup for *in situ* high-energy resolution fluorescence-detected XAS. A liquid jet is used to characterize the NPs during the *in situ* synthesis and the catalase mimetic activities. An X-ray emission spectrometer with vertical scattering geometry employing five analyzer crystals records the high-resolution data. A comparison between total fluorescence yield (TFY) and high-resolution (HERFD) XAS shows that the Ce 2p to 4f transitions and the fine structure in the 5d band can be resolved.

The spectral shape of transitions into the 4f orbitals of Ce is characteristic of the electron spin (S) and orbital angular momentum (L) of the ground state electronic structure, that is, the spin−orbit term ^{2S+1}L, because of the selection rules for photon-induced electron transitions.[16] Within this framework, the Ce^{4+} ion of configuration f^0 ($S = 0$) and the Ce^{3+} ion of configuration f^1 ($S = 1/2$) are assigned the symmetry terms ^1S and ^2F, respectively. A single configuration ionic picture has been shown to be insufficient to describe inner-shell spectroscopic data of ceria, and a multiconfiguration approach is necessary.[17,18] The electronic structure of Ce in CeO_2 with formal valence state of IV can be described as a mixture of f^0 and $f^1\underline{L}$ contributions (where $\underline{L}$ denotes a hole in a ligand orbital) thus considering orbital mixing and sharing of electron density between Ce and O (Supporting Information section 5). Such formalism implies that the system remains in a ^1S state independent of the f^0 and $f^1\underline{L}$ mixing ratio because the Ce f electron is spin-paired with a ligand electron. The resulting spectral shape is very different from a system with two distinct f^0 (Ce^{4+}, ^1S) and f^1 (Ce^{3+}, ^2F) sites where the spectrum presents the sum of the two sites. Oxygen-deficient $CeO_{2-\delta}$ may be described by an increased $f^1\underline{L}$ contribution in the presence of strong orbital mixing and an unchanged ^1S spin−orbit state. The importance of a multiconfiguration description of the Ce electronic structure has been emphasized for molecular complexes.[19,20] We show that this is also applied to ceria NPs. We note that it has been questioned whether the atomic-like Ce 4f orbitals are actually populated or whether the valence band has extended covalent states with f symmetry.[21] Many authors insist that the Ce 4f levels are empty in the ground state.[22,23] This unresolved controversy is irrelevant in the present context because our analysis by considering a $f^1\underline{L}$ configuration does not depend on the exact nature of the populated f density of electronic states.

RESULTS AND DISCUSSION

The process of $Ce(NO_3)_3 \cdot 6H_2O$ conversion into NPs and subsequent operation and aging at room temperature (RT) have been monitored *in situ* by the X-ray probe. Ce L_3 edge HERFD-XAS spectra recorded during the synthesis of colloidal CeO_2 NPs are shown in Figure 2a. Dominant spectral features can be assigned to Ce 2p to 5d transitions while weak pre-edge spectral features (Figure 2b) can be assigned to Ce 2p to Ce 4f transitions. The first recorded spectrum at the beginning of NP synthesis is that of the $Ce(NO_3)_3 \cdot 6H_2O$ precursor which presents one intense white line (peak A) typical for a Ce^{3+} ion.[24,25] On addition of the oxidizing agent hexamethyltetramine (HMT), the intensity of peak A decreases progressively while new peaks grow in intensity with time. The presence of several isosbestic points confirms that only two cerium species are involved in the formation of the NPs: Ce^{3+} (^2F) ions in $Ce(NO_3)_3 \cdot 6H_2O$ and Ce^{4+} (^1S) ions in CeO_2 NPs (Supporting Information section 4). The mixing of f^0 and $f^1\underline{L}$ configurations in ceria gives rise to two peak groups, C and B, that are often referred to as unscreened and screened final states, respectively.[18,26]

The pre-edge spectrum of $Ce(NO_3)_3 \cdot 6H_2O$ (Figure 2b, top) shows a group of spectral features. Upon formation of ceria NPs, the spectrum changes fundamentally and the final spectrum shows one single peak E. Atomic multiplet calculations of 2p to 4f transitions assuming a f^0 (^1S) and f^1 (^2F) ground state electron configuration for Ce^{4+} and Ce^{3+} ions, respectively, confirm the experimental observation (Figure 2b, bottom).[24] In the absence of spin and orbital angular momentum

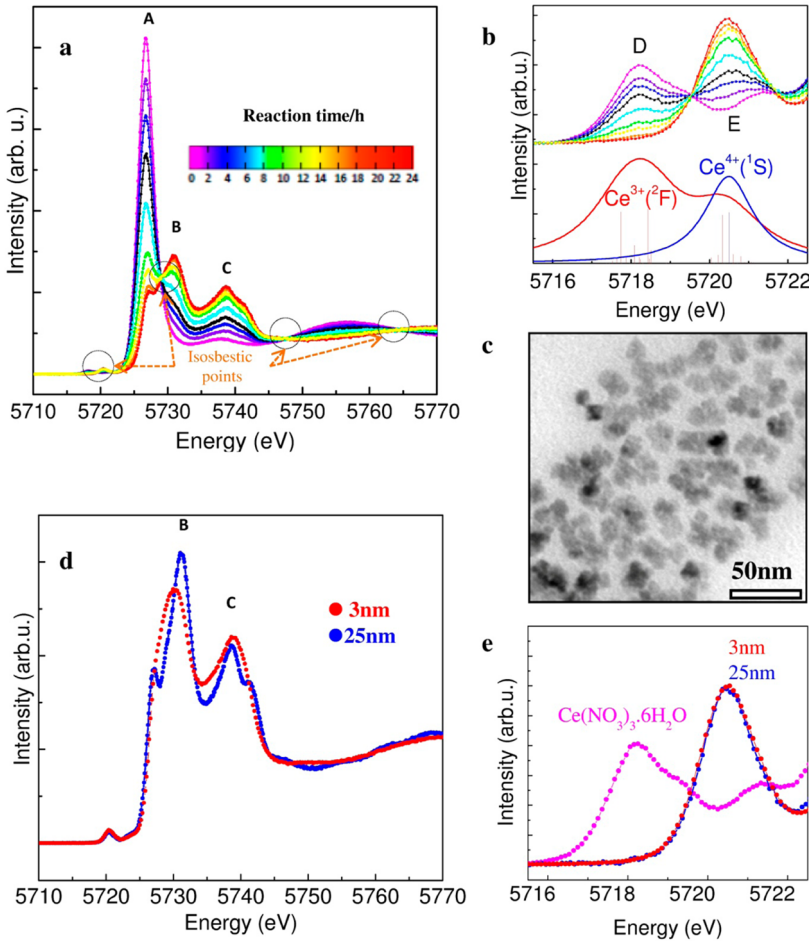

Figure 2. (a) Time-dependent high-energy resolution Ce L_3 XAS spectra recorded during the *in situ* synthesis of 10 nm CeO_2 NPs. (b) Enlargement of the pre-edge region (top) and atomic multiplet calculation for Ce^{3+} and Ce^{4+} ions (bottom). (c) TEM image of 10 nm CeO_2 NPs obtained from the synthesis. Scale bar, 50 nm. (d) Comparison between the Ce L_3 XAS spectra of 3 and 25 nm CeO_2. (e) Enlargement of the pre-edge spectra of 3 and 25 nm CeO_2 compared to the pre-edge spectrum of $Ce(NO_3)_3 \cdot 6H_2O$.

(^{1}S), only one transition is observed while a ^{2}F configuration results in a considerably richer spectral structure. The spectral changes observed at the pre-edge during the synthesis are thus in agreement with the oxidation of soluble Ce^{3+} (^{2}F) to insoluble Ce^{4+} (^{1}S) ions. The results show that all Ce ions are electron-paired in CeO_2 NPs with ^{1}S ground state symmetry.

Analysis of the TEM images gives an average size of 10 nm for the synthesized particles. We have studied smaller and larger particles with identical results for the Ce pre-edge spectrum (Figure 2e and Supporting Information section 6). We show here the synthesis for the 10 nm particles because the time evolution best matched the experimental time resolution of ~60 s, that is, the time per absorption scan.

We studied the effect of the NP size on the Ce electronic structure (Figure 2d). The pre-edge spectra of the 3, 10, and 25 nm CeO_2 NPs are identical and present one single peak characteristic of ^{1}S symmetry (Figure 2b,e). We do not observe any signature for an unpaired electron despite the drastic change of the surface to bulk ratio from approximately 65 to 10% between the 3 and 25 nm CeO_2 NPs. Structures B and C that relate to the Ce 5d electron density of states (DOS) show pronounced size dependence.[25] Sharper and more structured spectral features are observed for the 25 nm NPs than for the 3 nm NPs. The broader signature of the Ce 5d DOS for the 3 nm NPs may be explained by an increase in contribution from surface or near-surface Ce atoms to the spectra that superimpose on bulk-like spectra arising from Ce ions at the center of the NP.

We tested the catalytic activity of the ceria NPs by monitoring the catalase mimetic activities *in situ*, that is, monitoring the decomposition of hydrogen peroxide (H_2O_2) for the 3 nm and 25 nm CeO_2 NPs by HERFD-XAS (Figure 3). A comparison of the pH evolution for 3, 10, and 25 nm particles is shown in the Supporting Information section 7. The 3 nm NPs show the strongest change of pH, that is, the highest chemical activity, while the 25 nm NPs did not produce any detectable change of pH. For the 25 nm CeO_2 NPs, the HERFD-XAS spectra recorded before, immediately, and 20 h after adding H_2O_2 are identical, showing that the 25 nm

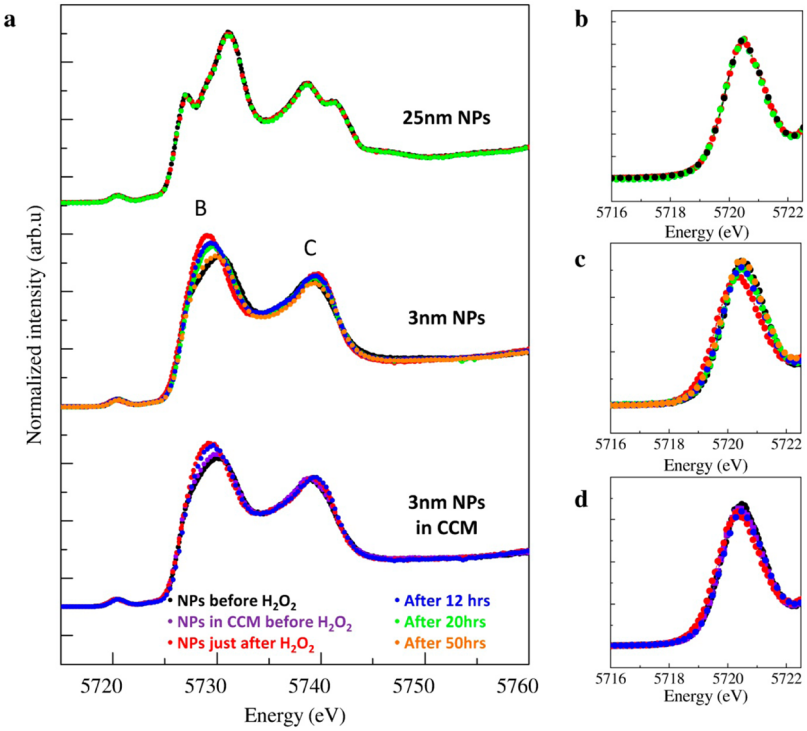

Figure 3. Catalase mimetic activity of the NPs. (a) Time-dependent Ce L_3 HERFD-XAS of the catalase mimetic activities of 25 nm CeO_2 (top), 3 nm CeO_2 (middle), and 3 nm CeO_2 dispersed in cell cultured medium (CCM) (bottom). (b–d) Insets show an enlargement of the pre-edge regions for the 25 nm CeO_2, 3 nm CeO_2, and 3 nm CeO_2 dispersed in CCM during the catalase mimetic activities.

CeO_2 NPs do not notably react with H_2O_2. In contrast, we observe rapid and significant changes of the HERFD-XAS spectra recorded for the 3 nm CeO_2 NPs when adding H_2O_2. The relative intensities of peaks B and C in the main edge region change. The pre-edge peak decreases slightly in intensity, and its energy position is shifted to lower energy. The pre-edge peak, however, remains as one strong resonance, leading us to conclude that Ce is in a ^1S state over the whole course of reaction. With time (after 12, 20, and 50 h), partial regeneration of the 3 nm CeO_2 NPs was observed, suggesting that the CeO_2 NPs revert to their original state.[6,27]

The degradation of H_2O_2 into H_2O and O_2 is hindered/accelerated with the absence/presence of the NPs which trap oxygen molecules, thereby favoring peroxide decomposition. The effects observed with the 3 nm NP colloidal solution also occur in biological media such as cell culture medium (CCM) (Figure 3, bottom). These results are relevant in view of proposed and existing applications of nano-CeO_2 as an antioxidant for neuroprotection,[28] treating cardiovascular disease,[29,30] and ophthalmology.[31] A better description of ceria NP activity on a quantum chemical level is a prerequisite for understanding possible toxic biological responses[32,33] in a bottom-up approach.

The redox activity of the ceria NPs without the creation of Ce^{3+} sites can be explained by Ce–O orbital mixing. This is illustrated by extracting an effective number of f electrons, n_f, from the experimental data (Figure 4a; Supporting Information section 5).[34,35] The number n_f provides a relative measure for the contribution of f^0 and $f^1\underline{L}$ configurations to the Ce electronic structure. On addition of H_2O_2, n_f increases rapidly from 0.48 to 0.58 and then it decreases progressively with time. The increase of n_f is accompanied by a shift of the pre-edge to lower energies. The two observations are consistent because a higher valence shell electron density is generally assumed to lower the edge energy due to charge screening effects.[36] The increase of n_f with a pre-edge which does not change shape indicates that the NPs accept electrons while remaining in ^1S symmetry. The progressive decrease of n_f with time suggests that the NPs are recovering their initial electronic structure and thus their capacity to autogenerate.[6,27,37]

The H_2O_2 degradation process results in acidification of the NP solution (Figure 4b). After H_2O_2 addition, the pH of the solution dropped from 4.8 to 3.6, indicating the proteic degradation of H_2O_2 into $2H^+ + O_2 + 2\,e^-$. The sudden decrease in pH occurs with an increase in n_f, suggesting that the reaction is catalyzed by the NPs. The control experiment (the same solution and reagents but without the CeO_2 NPs) does not show any detectable pH change. The short time scale and the fact that negative charge is transferred to ceria NPs during H_2O_2 degradation are in agreement with previously reported results.[6,28] The time scales for recovery of the pH and n_f are not correlated, indicating that the mechanisms are not directly linked.[37]

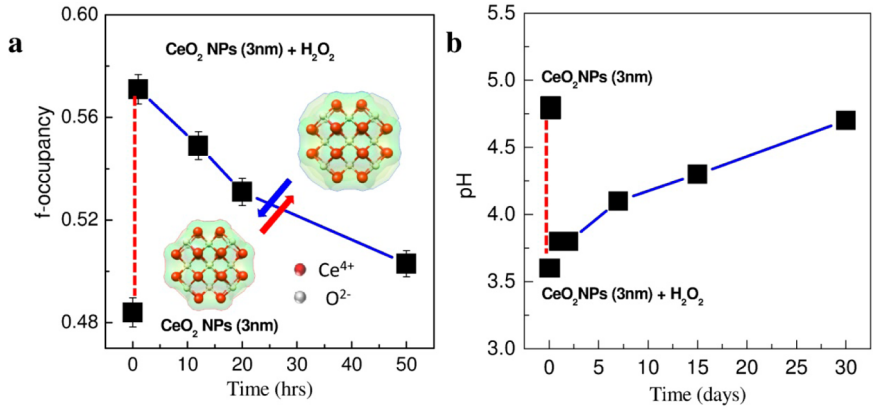

Figure 4. (a) Time dependence of the number of f electrons of the 3 nm CeO_2 NPs during the catalase mimetic activity. The electron sponge behavior of the 3 nm CeO_2 NPs is illustrated in a cartoon diagram. The green surface represents the electron density distribution that expands or contracts when receiving or releasing electrons. (b) Time dependence of the pH during the catalase mimetic activity of the 3 nm CeO_2 NPs.

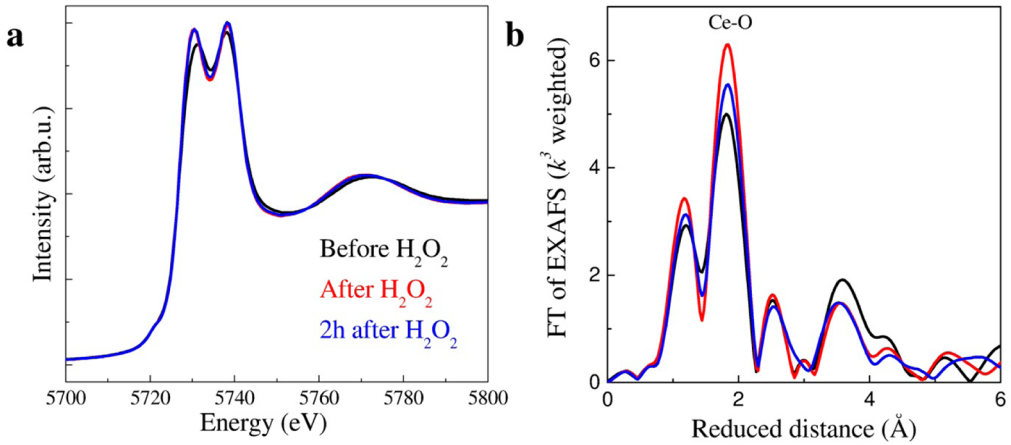

Figure 5. (a) Time-dependent Ce L_3 TFY XAS of the catalase mimetic activities of 3 nm CeO_2 showing the shift of the first EXAFS oscillation toward lower energy on addition of H_2O_2. (b) Superposition of the time-dependent k^3-weighted EXAFS Fourier transform (FT) magnitude spectra recorded during the catalase mimetic activities of 3 nm CeO_2.

We recorded the extended X-ray absorption fine structure (EXAFS)[38] during the catalase mimetic activity for the 3 nm CeO_2 NPs (Figure 5) using total fluorescence yield (TFY) detection. Just after the addition of H_2O_2, a shift of the energy position of the first EXAFS oscillation toward lower energy is observed in the absorption spectrum of the 3 nm CeO_2 NPs (Figure 5a). This sudden shift of the first EXAFS oscillation reflects a change in the Ce first coordination shell, that is, in the Ce−O bond distance. For a quantitative comparison of the local structure properties during the catalase mimetic activities, the data were Fourier transformed to *r* space, as shown in Figure 5b. The main peak of the Fourier transformed EXAFS corresponds to the Ce−O coordination shell. On addition of H_2O_2, the amplitude of the Fourier transformed EXAFS increases and it shifts slightly to higher radial distance. Fourier transformed fits of the first shell indicate an increase of the Ce−O distance from 2.28 to 2.32 Å just after addition of H_2O_2 (Supporting Information Table S1). The EXAFS data present an average over all Ce atoms in the X-ray beam; that is, the lengthening of the Ce−O bond is in agreement with a delocalized redistribution of charge density over the entire NP structure when oxygen vacancies are formed.[39,40]

CONCLUSIONS

We exclude the formation of a significant fraction of Ce^{3+} ($S = 1/2$) ions with decrease of the NP size and during catalase mimetic activity. The experiments under *in situ*/*operando* conditions show that the Ce 4f spin−orbit state is conserved, and we conclude that valence electrons populate orbitals that arise from Ce−O orbital mixing. The 3 nm NPs compensate for the excess charge by tuning their f^0 and $f^1\underline{L}$ mixing ratio and increasing the Ce−O distances, rather than favoring the localized surface reduction of Ce^{4+} (^1S) to Ce^{3+} (^2F) ions near an oxygen vacancy. This delocalized accommodation of charge invokes the picture of an electron sponge.

Unpaired electrons on Ce^{3+} sites are likely to play an important role in other systems under different conditions. We showed in this work that Ce^{3+} sites

are not necessary to account for the chemical activity of nanoceria under the conditions of the present study. We propose that the charge delocalization that we observed in the present study is generally relevant for ceria, and we conclude that a description of the activity on a quantum chemical level needs to include a Ce spin-conserving mechanism.

Our results highlight the complexity and remarkable plasticity of the electronic structure of ceria at the nanoscale and the resulting ability to tune electronic states of inorganic materials. Understanding CeO_2 NP chemical properties requires consideration of the entire NP including morphology and chemical environment.

METHODS

Synthesis of Colloidal CeO_2 Nanoparticles. Cerium(III) nitrate hexahydrate, cerium(IV) oxide nanopowder <25 nm particle size (BET), tetramethylammonium solution ACS reagent (1.0 ± 0.02 M in H_2O), hexamethylenetetramine ACS reagent, ethanol ACS reagent (absolute alcohol ≥99.8%) without additive, hydrogen peroxide ACS reagent, 30 wt % in H_2O, phosphate buffered saline, pH 7.4, and fetal bovine serum (FBS) were purchased from Sigma Aldrich.

3 nm CeO_2 NPs:. In a first step, 10 mM of cerium(III) nitrate hexahydrate was dissolved in 100 mL of absolute ethanol at room temperature. The solution was left under stirring for about 30 min. To the 100 mL solution was added 1 mL of TMAOH (1.0 ± 0.02 M in H_2O) at a final concentration of 10 mM, and the mixture was left under stirring.

10 nm CeO_2 NPs:. In a first step, 10 mM of cerium(III) nitrate hexahydrate was dissolved in 90 mL of absolute ethanol at room temperature. To this solution was added 10 mL of HMT (1 M) at a final concentration of 100 mM, and the solution was left under stirring.

For all samples, NPs were purified by centrifugation and resuspended in aqueous solutions of either 10 mM TMAOH (in the case of 3 nm NPs) or 100 mM HMT (in the case of 10 nm NPs) which act as stabilizers.

Catalase Mimetic Activity of the CeO_2 NPs. To a 100 mL solution of colloidal (3 and 25 nm) CeO_2 (final Ce concentration = 10 mM) under stirring was added 1 mL of H_2O_2 at physiologically relevant concentration (final H_2O_2 concentration = 4 μM), and the mixture was characterized *in situ* by XAS measurements using the jet-flow setup.

The 3 nm CeO_2 NPs and a model of cell culture media consisting on phosphate buffer saline (PBS) supplemented with 10% (v/v) FBS were mixed (1:10 by volume) and placed under stirring for more than 10 h. To this solution was added 1 mL of H_2O_2 at a final concentration of 10 mM, and the mixture was characterized *in situ* by XAS measurements in the jet-flow setup.

High-Energy Resolution Fluorescence-Detected X-ray Absorption Spectroscopy (HERFD-XAS) and Extended X-ray Absorption Fine Structure (EXAFS) Analysis. The experiment was performed at beamline ID26 of the European Synchrotron Radiation Facility (ESRF) in Grenoble.[41] The incident energy was selected using the ⟨111⟩ reflection from a double Si crystal monochromator. Rejection of higher harmonics was achieved by three Si mirrors working under total reflection. The incident photon flux was monitored by detecting the X-rays scattered from a foil using a photodiode. Five spherically bent (R = 1 m) Ge crystal analyzers in ⟨331⟩ reflection were chosen suitable for the detection of the $L\alpha_1$ emission line of Ce (4839 eV). The combined energy bandwidth was 0.9 eV. Sample, analyzer crystal, and photon detector (avalanche photodiode) were arranged in a vertical Rowland geometry (Figure 1). The HERFD-XAS spectra were recorded at scattering angles covering 70−110° in the horizontal plane. The EXAFS spectra were measured in fluorescence mode by placing a photodiode near the sample. The measuring conditions were carefully chosen to avoid radiation damage due to the exposure of the CeO_2 NPs to the X-ray. The experimental error in the X-ray spectra is dominated by the statistical error of the single photon detection. It is on the order of the marker size in the figures (see also the Supporting Information).

For the *in situ* synthesis, XAS spectra of the precursor were first recorded before the addition of the oxidizing agent. For the catalase mimetic activity, XAS spectra of the 3, 25, and 3 nm NPs dispersed in CCM were first recorded before the addition of H_2O_2.

Conflict of Interest: The authors declare no competing financial interest.

Acknowledgment. We thank A. Kotani and N. G. Bastùs for discussions.

Supporting Information Available: Additional information includes sample characterizations by TEM, UV−vis spectroscopy, pH study, XRD and EXAFS, radiation damage study, qualitative analysis using iterative transformation factor analysis (ITFA) and estimation of the number of 4f electrons. This material is available free of charge *via* the Internet at http://pubs.acs.org.

REFERENCES AND NOTES

1. Trovarelli, A. Catalytic Properties of Ceria and CeO_2-Containing Materials. *Catal. Rev.* **1996**, *38*, 439–520.
2. Chueh, W. C.; Falter, C.; Abbott, M.; Scipio, D.; Furler, P.; Haile, S. M.; Steinfeld, A. High-Flux Solar-Driven Thermochemical Dissociation of CO_2 and H_2O Using Nonstoichiometric Ceria. *Science* **2010**, *330*, 1797–1801.
3. Carrettin, S.; Concepcion, P.; Corma, A.; Nieto, J. M. L.; Puntes, V. F. Nanocrystalline CeO_2 Increases the Activity of Au for CO Oxidation by Two Orders of Magnitude. *Angew. Chem., Int. Ed.* **2004**, *43*, 2538–2540.
4. Steele, B. C. H.; Heinzel, A. Materials for Fuel-Cell Technologies. *Nature* **2001**, *414*, 345–352.
5. Deluga, G. A.; Salge, J. R.; Schmidt, L. D.; Verykios, X. E. Renewable Hydrogen from Ethanol by Autothermal Reforming. *Science* **2004**, *303*, 993–997.
6. Celardo, I.; Pedersen, J. Z.; Traversa, E.; Ghibelli, L. Pharmacological Potential of Cerium Oxide Nanoparticles. *Nanoscale* **2011**, *3*, 1411–1420.
7. Karakoti, A. S.; Monteiro-Riviere, N. A.; Aggarwal, R.; Davis, J. P.; Narayan, R. J.; Self, W. T.; McGinnis, J.; Seal, S. Nanoceria as Antioxidant: Synthesis and Biomedical Applications. *JOM* **2008**, *60*, 33–37.
8. Sun, C. W.; Li, H.; Chen, L. Q. Nanostructured Ceria-Based Materials: Synthesis, Properties and Applications. *Energy Environ. Sci.* **2012**, *5*, 8475–8505.
9. Lermontov, A. S.; Ivanov, V. K.; Yakimova, M. S.; Baranchikov, A. E.; Polezhaeva, O. S.; Tret'yakov, Y. D. Size Effect in CO Oxidation on CeO_{2-x} Nanoparticles. *Dokl. Chem.* **2010**, *430*, 4–7.
10. Esch, F.; Fabris, S.; Zhou, L.; Montini, T.; Africh, C.; Fornasiero, P.; Comelli, G.; Rosei, R. Electron Localization Determines Defect Formation on Ceria Substrates. *Science* **2005**, *309*, 752–755.
11. Jerratsch, J. F.; Shao, X.; Nilius, N.; Freund, H. J.; Popa, C.; Ganduglia-Pirovano, M. V.; Burow, A. M.; Sauer, J. Electron Localization in Defective Ceria Films: A Study with Scanning-Tunneling Microscopy and Density-Functional Theory. *Phys. Rev. Lett.* **2011**, *106*, 246801.
12. Deshpande, S.; Patil, S.; Kuchibhatla, S. V. N. T.; Seal, S. Size Dependency Variation in Lattice Parameter and Valency States in Nanocrystalline Cerium Oxide. *Appl. Phys. Lett.* **2005**, *87*, 133113.
13. Zhang, F.; Wang, P.; Koberstein, J.; Khalid, S.; Chan, S. W. Cerium Oxidation State in Ceria Nanoparticles Studied

with X-ray Photoelectron Spectroscopy and Absorption Near Edge Spectroscopy. *Surf. Sci.* **2004**, *563*, 74–82.
14. Hämäläinen, K.; Siddons, D. P.; Hastings, J. B.; Berman, L. E. Elimination of the Inner-Shell Lifetime Broadening in X-ray-Absorption Spectroscopy. *Phys. Rev. Lett.* **1991**, *67*, 2850–2853.
15. Glatzel, P.; Bergmann, U. High Resolution 1s Core Hole X-ray Spectroscopy in 3d Transition Metal Complexes—Electronic and Structural Information. *Coord. Chem. Rev.* **2005**, *249*, 65–95.
16. Cowan, R. D. *The Theory of Atomic Structure and Spectra*; University of California Press: Berkeley, CA, 1981.
17. Gunnarsson, O.; Schonhammer, K. Electron Spectroscopies for Ce Compounds in the Impurity Model. *Phys. Rev. B* **1983**, *28*, 4315–4341.
18. Kotani, A.; Shin, S. Resonant Inelastic X-ray Scattering Spectra for Electrons in Solids. *Rev. Mod. Phys.* **2001**, *73*, 203–246.
19. Booth, C. H.; Walter, M. D.; Daniel, M.; Lukens, W. W.; Andersen, R. A. Self-Contained Kondo Effect in Single Molecules. *Phys. Rev. Lett.* **2005**, *95*, 267202.
20. Kerridge, A.; Kaltsoyannis, N. All-Electron Caspt2 Study of Ce(Eta(8)-C8H6)(2). *C.R. Chim.* **2010**, *13*, 853–859.
21. Wuilloud, E.; Delley, B.; Schneider, W. D.; Baer, Y. Spectroscopic Evidence for Localized and Extended F-Symmetry States in CeO_2. *Phys. Rev. Lett.* **1984**, *53*, 202–205.
22. Goubin, F.; Rocquefelte, X.; Whangbo, M. H.; Montardi, Y.; Brec, R.; Jobic, S. Experimental and Theoretical Characterization of the Optical Properties of CeO_2, $SrCeO_3$, and Sr_2CeO_4 Containing Ce4+ (F(0)) Ions. *Chem. Mater.* **2004**, *16*, 662–669.
23. Sham, T. K.; Gordon, R. A.; Heald, S. M. Resonant Inelastic X-ray Scattering at the Ce L-3 Edge of $CePO_4$ and CeO_2: Implications for the Valence of CeO_2 and Related Phenomena. *Phys. Rev. B* **2005**, *72*, 035113.
24. Kvashnina, K. O.; Butorin, S. M.; Glatzel, P. Direct Study of the f-Electron Configuration in Lanthanide Systems. *J. Anal. At. Spectrom.* **2011**, *26*, 1265–1272.
25. Paun, C.; Safonova, O. V.; Szlachetko, J.; Abdala, P. M.; Nachtegaal, M.; Sa, J.; Kleymenov, E.; Cervellino, A.; Krumeich, F.; van Bokhoven, J. A. Polyhedral CeO_2 Nanoparticles: Size Dependent Geometrical and Electronic Structure. *J. Phys. Chem. C* **2012**, *116*, 7312–7317.
26. Bianconi, A.; Marcelli, A.; Dexpert, H.; Karnatak, R.; Kotani, A.; Jo, T.; Petiau, J. Specific Intermediate-Valence State of Insulating 4f Compounds Detected by L_3 X-ray Absorption. *Phys. Rev. B* **1987**, *35*, 806–812.
27. Pirmohamed, T.; Dowding, J. M.; Singh, S.; Wasserman, B.; Heckert, E.; Karakoti, A. S.; King, J. E. S.; Seal, S.; Self, W. T. Nanoceria Exhibit Redox State-Dependent Catalase Mimetic Activity. *Chem. Commun.* **2010**, *46*, 2736–2738.
28. Das, M.; Patil, S.; Bhargava, N.; Kang, J. F.; Riedel, L. M.; Seal, S.; Hickman, J. J. Auto-catalytic Ceria Nanoparticles Offer Neuroprotection to Adult Rat Spinal Cord Neurons. *Biomaterials* **2007**, *28*, 1918–1925.
29. Niu, J. L.; Azfer, A.; Rogers, L. M.; Wang, X. H.; Kolattukudy, P. E. Cardioprotective Effects of Cerium Oxide Nanoparticles in a Transgenic Murine Model of Cardiomyopathy. *Cardiovasc. Res.* **2007**, *73*, 549–559.
30. Pagliari, F.; Mandoli, C.; Forte, G.; Magnani, E.; Pagliari, S.; Nardone, G.; Licoccia, S.; Minieri, M.; Di Nardo, P.; Traversa, E. Cerium Oxide Nanoparticles Protect Cardiac Progenitor Cells from Oxidative Stress. *ACS Nano* **2012**, *6*, 3767–3775.
31. Chen, J. P.; Patil, S.; Seal, S.; McGinnis, J. F. Rare Earth Nanoparticles Prevent Retinal Degeneration Induced by Intracellular Peroxides. *Nat. Nanotechnol.* **2006**, *1*, 142–150.
32. Xia, T.; Kovochich, M.; Liong, M.; Madler, L.; Gilbert, B.; Shi, H. B.; Yeh, J. I.; Zink, J. I.; Nel, A. E. Comparison of the Mechanism of Toxicity of Zinc Oxide and Cerium Oxide Nanoparticles Based on Dissolution and Oxidative Stress Properties. *ACS Nano* **2008**, *2*, 2121–2134.
33. Hussain, S.; Al-Nsour, F.; Rice, A. B.; Marshburn, J.; Yingling, B.; Ji, Z. X.; Zink, J. I.; Walker, N. J.; Garantziotis, S. Cerium Dioxide Nanoparticles Induce Apoptosis and Autophagy in Human Peripheral Blood Monocytes. *ACS Nano* **2012**, *6*, 5820–5829.
34. Booth, C. H.; Kazhdan, D.; Werkema, E. L.; Walter, M. D.; Lukens, W. W.; Bauer, E. D.; Hu, Y. J.; Maron, L.; Eisenstein, O.; Head-Gordon, M.; *et al.* Intermediate-Valence Tautomerism in Decamethylytterbocene Complexes of Methyl-Substituted Bipyridines. *J. Am. Chem. Soc.* **2010**, *132*, 17537–17549.
35. Rueff, J. P.; Itié, J. P.; Taguchi, M.; Hague, C. F.; Mariot, J. M.; Delaunay, R.; Kappler, J. P.; Jaouen, N. Probing the Gamma-Alpha Transition in Bulk Ce under Pressure: A Direct Investigation by Resonant Inelastic X-ray Scattering. *Phys. Rev. Lett.* **2006**, *96*, 237403.
36. Wilke, M.; Schmidt, C.; Farges, F.; Malavergne, V.; Gautron, L.; Simionovici, A.; Hahn, M.; Petit, P. E. Structural Environment of Iron in Hydrous Aluminosilicate Glass and Melt-Evidence from X-ray Absorption Spectroscopy. *Chem. Geol.* **2006**, *229*, 144–161.
37. Heckert, E. G.; Karakoti, A. S.; Seal, S.; Self, W. T. The Role of Cerium Redox State in the Sod Mimetic Activity of Nanoceria. *Biomaterials* **2008**, *29*, 2705–2709.
38. Rehr, J. J.; Albers, R. C. Theoretical Approaches to X-ray Absorption Fine Structure. *Rev. Mod. Phys.* **2000**, *72*, 621–654.
39. Shoko, E.; Smith, M. F.; McKenzie, R. H. Charge Distribution near Bulk Oxygen Vacancies in Cerium Oxides. *J. Phys.: Condens. Matter* **2010**, *22*, 223201.
40. Kang, Z. C.; Eyring, L. The Structural Basis of the Fluorite-Related Rare Earth Higher Oxides. *Aust. J. Chem.* **1996**, *49*, 981–996.
41. Gauthier, C.; Sole, V. A.; Signorato, R.; Goulon, J.; Moguiline, E. The ESRF Beamline ID26: X-ray Absorption on Ultra Dilute Sample. *J. Synchrotron Radiat.* **1999**, *6*, 164–166.